Soluble surfactant spreading: How the amphiphilicity sets the Marangoni hydrodynamics

Sébastien Le Roux,[1] Matthieu Roché,[2] Isabelle Cantat,[1] and Arnaud Saint-Jalmes[1]
[1]*Institut de Physique de Rennes, UMR 6251 CNRS-Université Rennes 1, Rennes, France*
[2]*Laboratoire Matière et Systèmes Complexes, UMR 6251 CNRS-Université Paris 7, Paris, France*
(Received 14 June 2015; published 6 January 2016)

Amphiphiles are molecules combining hydrophilic and hydrophobic parts. The way they arrange in bulk and at interfaces is related to the balance between these two parts, and can be quantified by introducing the critical micellar concentration (cmc). Amphiphiles (also named "surfactants") are also at the origin of dynamical effects: local gradients of interfacial concentrations create the so-called Marangoni flows. Here we study the coupling between the molecule amphiphilicity and these Marangoni flows. We investigate in detail a spreading configuration, where a local excess of surfactants is locally sustained, and follow how these surfactants spread at the interface and diffuse in bulk. We have measured the features of this flow (maximal distance and maximal speed), for different types of surfactant, and as a function of all experimentally available parameters, as well as for two different configurations. In parallel, we propose a detailed hydrodynamical model. For all the measured quantities, we have found a good agreement between the data and the model, evidencing that we have captured the key mechanisms under these spreading experiments. In particular, the cmc turns out to be—as for the static picture of a surfactant—a key element even under dynamical conditions, allowing us to connect the molecule amphiphilicity to its ability to create Marangoni flows.

DOI: 10.1103/PhysRevE.93.013107

I. INTRODUCTION

Amphiphilic molecules are made by associating two parts of opposite nature, one being *hydrophobic* and the other *hydrophilic*. The chemical structures of these two parts set the balance between hydrophobicity and hydrophilicity, i.e., the *amphiphilicity* of the molecule. These two opposite parts actually differ by their solubility in water. In water, any added molecule disturbs the local organization of the surrounding water molecules. It is the amplitude of the distortion of this bond network which dictates the solubility of the added molecule. This interaction is known as the hydrophobic effect [1–3]. As a consequence, all chemicals have a critical concentration for solubility, describing the maximal amount which can be solubilized in water, before phase separation. Molecules with low solubility—such as alkane chains—are therefore considered to be hydrophobic. By assembling a hydrophilic moiety to such hydrophobic molecules, one can balance the hydrophobic effect and eventually obtain an amphiphilic compound.

This ambivalent structure of amphiphiles is at the origin of various specific behaviors. In terms of solubility, gaining an amphiphilic behavior has a strong impact. As long as $T > T_K$, where T_K is the Krafft temperature of the molecule [4,5], the solubility increases by several orders of magnitude, when compared to the one of the hydrophobic part. The origin of this effect is linked to the ability for amphiphiles to form finite-size aggregates, called micelles [4,5]. The bulk concentration above which the number of micelles increases sharply is called the "critical micelle concentration" (cmc). In parallel to the formation of micelles in bulk, amphiphiles can also optimize their interaction with water by adsorbing at free interfaces. As a consequence, the gas-solution interfacial tension is reduced; hence, amphiphiles are also named "surfactants" in relation to their activity at surfaces. From an equilibrium point of view, the bulk concentration, surface concentration, and surface tension are fully imbricated. The occurrence of micelles in bulk above the cmc corresponds to a saturation of the interfacial concentration and surface tension. All these features can be compiled within various theoretical frameworks, such as the widely used one from Gibbs [4–7]. In this equilibrium picture, the impact of the amphiphilicity is known [4,5,8]; as a central landmark, it is found that the more hydrophobic a molecule, the lower its cmc. As well, the cmc of a given molecule depends on experimental parameters, such as the temperature or the presence of added salt (the latter will be investigated below). From a practical point of view, it is these specificities in bulk and at interfaces which make surfactants the ideal candidate for stabilizing dispersions, su foams and emulsions.

Together with the above self-assembled features in bulk and at interfaces, amphiphiles are also at the origin of a dynamical effect, known as the Marangoni effect. Heterogeneities in the distribution of surfactant molecules at the interface between two fluids triggers a Marangoni flow, i.e., the bulk flow of both phases due to a gradient of their interfacial tension [9,10]. Fluid flows induced by gradients of interfacial tension have received a great deal of attention, as they are encountered in different situations, such as transport phenomena in lipid nanotubes [11,12], the formation of lipid tethers [13], the stability and dynamics of thin liquid films in foams and emulsions [14,15], capillary locomotion of insects [16–19], surfactant replacement therapy for neonates suffering from respiratory distress syndrome [20,21], coating and printing processes [22,23], or the control of water evaporation [24,25]. In all these cases, taking into account a Marangoni effect is a key point in the understanding.

From a general point of view, two kinds of concentration-induced Marangoni flows can be distinguished. In the first case, surface tension gradients are created in systems with a fixed amount of surfactants, by varying locally the area of an air-solution interface or the concentration. This is what happens, for instance, when considering fluctuations of a foam liquid lamellae, or—in a more controlled way—when using

an overflowing cylinder [26–28]. In the second case, surface tension gradients are induced exogenously by adding extra surfactants to an initial system. A simple example of the latter situation is the controlled deposition of a solution of surfactants on a layer of a liquid, having a different surface tension. This problem has been extensively studied, both experimentally and through simulations, for the case of surfactants insoluble in the bulk phase [29–37]. In that case, the molecules spread on the interface as a result of the Marangoni stresses, together with a front of vertical deformation of the interface.

In comparison, and despite its relevance to real situations, the study of spreading flow due to soluble surfactants has received less attention. A large part of past studies deal with the spreading of soluble liquids (mostly alcohols) on water, i.e., systems without cmc and micelles [38–43]. When solutions of soluble surfactants are considered, mostly numerical simulations have been done [44–46], whereas experimental studies often focused on transient behavior, especially on front propagation [47–49]. Moreover, experimental results were often collected for very thin films (less than 1 mm in thickness), adding complexities such as the occurrence of fingering instabilities [50,51]. Finally, experiments were also often performed in confined and/or small size vessels [50,52].

All together, these works tend to show that the possibility to have some transfer of amphiphiles from the interface to the bulk can balance the Marangoni stress, and can actually change the spreading dynamics. Qualitatively, for soluble species, it is clear that there has to be a competition between interfacial spreading (driven by the hydrophobic part), and solubilization in bulk (driven by the hydrophilic part). Although the links between amphiphilicity and equilibrium features in bulk and at interfaces have been widely studied, it remains to elucidate how the hydrophilic-hydrophobic balance of a surfactant drives the Marangoni spreading flows. In that respect, the quantitative scale relevant to the description of amphiphilicity under dynamical conditions must be identified.

To solve some of these issues, we recently published first results on the exogenous spreading of a soluble surfactant [53]. It was shown that, for a soluble surfactant, the spreading is limited in distance, and this distance depends on the surfactant structure. We proposed a scaling description which was partially validated by experiments. Nonetheless, more work was needed to understand thoroughly these features. In that spirit, we report here a new set of experimental and theoretical results on the dynamics of spreading with soluble surfactants. In particular, we generalize the problem to a new longitudinal configuration, and study the scaling regimes for the flow velocity in both axisymmetric and longitudinal configurations. Also, the spreading experiments are generalized to another type of surfactants (nonionic ones), and we report new results on the effect of glycerol, used to tune the viscosity. We also discuss experimental artefact and limitations, as well as the role of insoluble impurities. Together with the experimental results, we propose a mathematical model for the model, and highlight the excellent agreement between this model and our data, thus proving that we are able to understand the links between the finite surfactant amphiphilicity and the finite characteristics of the Marangoni spreading flow.

TABLE I. Table of physicochemical properties of the different surfactant solutions.

Surfactant solution	Surface tension (mN/m)	cmc (10^{-3} M)
C_{10}TAB	39.5	65
C_{12}TAB	39	14
C_{14}TAB	38	3.6
SDS	35	8.1
C_8E_5	35	9.2
$C_{10}E_5$	38	0.9

II. EXPERIMENT

A. Chemicals

We performed experiments using the ionic surfactants sodium dodecyl sulfate (SDS, i.e., $C_{12}NaSO_4$), decyltrimethylammonium bromide (C_{10}TAB), dodecyltrimethylammonium bromide (C_{12}TAB), and tetradecyltrimethylammonium bromide (C_{14}TAB). We also used two nonionic surfactants—pentaethylene glycol monooctyl ether C_8E_5 and pentaethylene glycol monodecyl ether $C_{10}E_5$—whose cmc values are on the same order as the cmc of the ionic surfactants. All chemicals were purchased from Sigma-Aldrich, with a purity greater than 99%. They are all dissolved in ultrapure water (Millipore water).

The cmc values and the surface tension above the cmc at equilibrium are given in Table I. Note that the cmc varies over almost two orders of magnitude, while the corresponding surface tensions are different by less than 5 mN m^{-1} [54–56].

In the spreading experiments, all the surfactant solutions have concentrations above the cmc (from twice the cmc up to 30 times the cmc, as shown in the following sections). Moreover, for tests on the role of impurities, myristic acid—an insoluble fatty acid, of chemical formula ($C_{14}H_{28}O_2$)—is added to set the amount of insoluble species present in the surfactant solution. Glycerol is used to tune the bulk viscosity of these solutions.

B. Type of experiments and setups

The principle of our experiment consists of a continuous deposition, at constant flow rate Q, of a concentrated surfactant solution on top of a aqueous layer. We use a high-precision syringe pump ("PhD Ultra" from Harvard Apparatus) to sustain this localized steady input of surfactant, with typical molar flow rates on the order of μmol/s. The solution is deposited through a stainless steel needle (diameter $d_n = 3 \times 10^{-3}$ m). Then, as discussed below, we monitor how this excess is hydrodynamically redistributed. The liquid pool is also pure water (Millipore range). In some cases, it can also contain surfactants to set the initial surface tension of the reservoir, or glycerol to tune the bulk viscosity of this reservoir. All the experiments are done at room temperature ($T = 21\,^{\circ}$C).

We used liquid tanks of various sizes and shapes, with areas A of 79, 227, 650, 875, 1600, and 8000 cm^2. The thickness of the liquid layer in the tank was between 1 and 5 cm. Thinner layers led to the establishment of different kinds of flow, similar to those observed when surfactants spread on thin films [36].

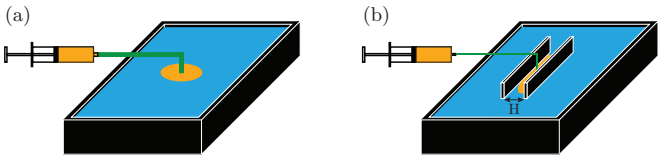

FIG. 1. Experimental configurations. (a) Axisymmetric spreading. (b) Longitudinal spreading.

Experiments are performed in two deposition configurations. The first one corresponds to a pointlike source, providing axisymmetric spreading (Fig. 1). The second type of geometries allows us to study a longitudinal spreading. It is performed in a rectangular container 2 meters long and 35 cm wide. Inside the reservoir, two spacer sheets are placed to select any width from 3 to 30 cm (Fig. 1). Then, depending on the selected width, one or multiple point sources (up to 8) are use to create a homogeneous deposition along the width (point sources are placed every 3 cm).

C. Typical observations of the Marangoni flow: Finite spreading distances and velocities

A central point of our measurements is that we dope the surfactant solutions with tracers to visualize the macroscopic flow boundaries and to measure the local velocity. In the following experiments, we mostly use oil droplets for the tracers. Basic vegetal oils (such as sunflower, rapeseed, or olive oil) are mixed to the surfactant solutions to produce oil-in-water emulsions, using an Ultra-Turrax or a two-syringe device. The fraction of oil and solution are equal, so that we prepare a 50/50 oil-in-water emulsion. The oil droplets have diameters on the order of 10 μm: with such a size and oil fraction, the deposited dispersion remains fluid with a low viscosity, while it already looks milky. As well, this emulsion remains stable for at least a couple of hours, as the adsorbed surfactants prevent fast coarsening or coalescence.

Once oil droplets are added, typical flow patterns are observed, as shown in Fig. 2 for the two configurations; clear separations and limits are revealed from the variations of the grey level. Qualitatively, the white zone corresponds to high surface density of droplets, while the dark zone corresponds to low ones. As the experiment runs in a continuous mode with a constant imposed flux, this implies a low velocity of droplets in white zones, whereas the tracers flow at high velocity in dark zones. Thus, along a radius starting from the deposition locus [Fig. 2(a)], we first observe a small white region of radius r_s (high density and low speed of tracers), followed by a transparent region (low density and high speed of tracers) up to a radius R, and the density of tracers re-increases after R. Note the characteristic vortex patterns occurring just after R, arising from hydrodynamical instabilities (the study of which is beyond the scope of this article). Far from these recirculation patterns located around R, the surface appears dark as no tracers have reached these distances. The same phenomenology, with clear separation between different regimes, is recovered in the longitudinal configuration, allowing us to determine a typical distance L [Fig. 2(b)].

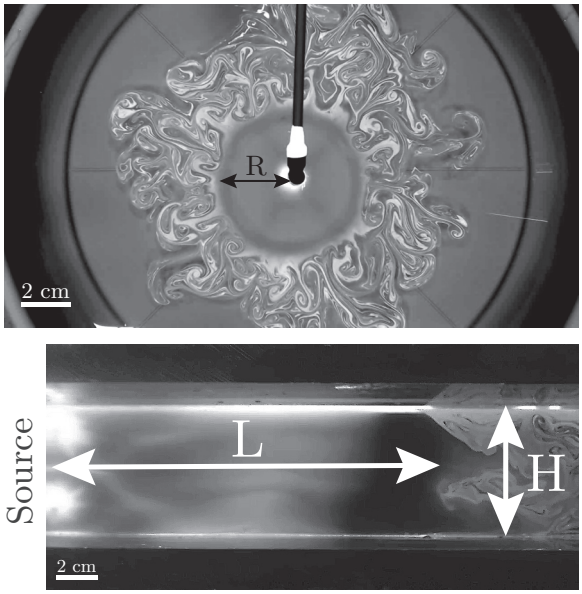

FIG. 2. Typical top views in the axisymmetric (top) and rectilinear (bottom) configurations. The Marangoni flow extends over a distance R in the axisymmetric configuration and over a distance L in the rectilinear configuration. The dimension are $R = 2.6$ cm, $L = 9.6$ cm, $H = 5$ cm.

We can therefore infer that the tracers are only transported to a finite distance, located at R and L in Fig. 2. Above R or L, the Marangoni flow has stopped, and the tracers become free to float on top of the fluid layer. With such definitions, the values R and L can then be measured as a function of the various parameters.

We had shown previously that these oil droplets, acting as tracers, were passive from a hydrodynamical point of view over the typical timescale of our measurements (for instance, solid particles simultaneously deposited with the surfactants gave the same results) [53]. As a new test, we used gas bubbles as tracers. By adding gas bubbles to the surfactant solution, we have studied how foams spread on pure water. Foams were also generated with the two-syringe device, allowing us to have different initial liquid fractions (from 0.05 to 0.2), while aging of the foam provides different bubble sizes (within the range of hundreds of microns). In all the cases of bubble sizes and liquid fractions, the same phenomenology and flow patterns are recovered, definitively showing that the distance of spreading is independent of the tracer.

Importantly, note that the pictures of Fig. 2 correspond to a steady state, obtained after a transient of typically 30 seconds. In Fig. 3(a), we show typical evolutions of $R(t)$ for three different tank areas, showing the initial transient, the steady state—where R and L are measured—and a final regime where $R(t)$ eventually decreases. The reasons for this final decrease are discussed below.

To go further on the flow characterization, we add a measurement of the local speed of the tracers. In practice, we used a high-speed camera to monitor the motion of the droplet at the surface. A Phlox light was installed under the tank. A Photron Fastcam mounted with a 20-cm-long bellow and a reverse 50-mm Nikon camera lens was used to record from

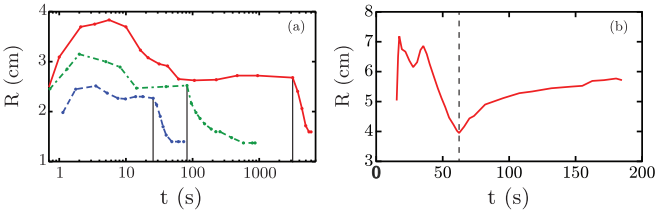

FIG. 3. (a) Radius R as a function of time. $V = 0{,}8$ l. $Q = 1$ μmol s^{-1}. Dashed line: $S = 79$ cm^2. Dashed-dotted line: $S = 227$ cm^2. Solid line: $S = 650$ cm^2. Vertical lines: times when vortices stop at the interface and when oil droplets get packed, coinciding with the decrease of R. (b) Spreading radius R as a function of time, in the overflowing setup (vessel radius $R_{\text{vessel}} = 9.45$ cm). Beginning of overflowing at $t = 62$ s. $V = 2$ l. $Q = 1$ μmol s^{-1}.

above at 3000 images/s the oil droplets' motion at any location. With this configuration, the field of view is 2 mm wide. As a consequence, the full tracers' trajectories are obtained by translating the recording setup along the spreading axis. The resulting velocity profiles are consistent with the ones shown in [53], with high velocities within the spreading zone, separated by an acceleration close to the deposition point, and deceleration occurring slightly before R. In the following, we report the maximum velocity value; it is respectively located at a radius $r \approx 0.3R$ and length $l \approx 0.5L$ in the axisymmetric and longitudinal configurations.

There is a practical limit in terms of accuracy for determining the spreading boundaries. As explained, the grey level variations correspond to speed variations. Thus, sharp velocity gradients and high velocities in the spreading region are required to get accurate values of R and L. The experiments show that, for given parameter ranges, the velocity is no longer high enough to optically detect the frontiers of the spreading area, especially the starting (acceleration) position (r_s) and ending (deceleration) position (R or L). Thus, as shown below, our measurements of spreading distances will be limited as soon as the flow velocity gets too low. Still, we will be able to obtain some values for the maximal velocities under these conditions.

D. Time evolution: Accumulation of tracers and insoluble species

In this section, we discuss two different phenomena occurring with time—accumulation of tracers and insoluble species at the interface—and determine their actual role on the finite spreading and on the evolution seen on Fig. 3(a).

In [53], we already proposed that the main source for the final decrease of R is linked to the finite area of the container and to the accumulation of tracers populating this area. Indeed, the free area available for the floating droplets decreases with time, as more and more droplets are deposited. At some time, these droplets gets packed, and all the surface around the spreading area appears white; observations showed that it is when the droplets have fully covered the free interface that they start to crop the spreading zone, so that R starts to decrease. The data of Fig. 3(a) confirm that we can control this effect by changing the area of the container. To fully investigate this effect, a new experiment was performed, using an overflowing configuration. The point is to perform the experiment in a vessel, almost full of water and at the limit of overflowing. The vessel radius must remain larger (here, $R_{\text{vesell}} = 9.45$ cm) than the spreading distance [$R \sim 6.5$ cm at the flow rate chosen in Fig. 3(b)]. Therefore, during a first regime [about 60 s of deposition in Fig. 3(b)], there is no overflow, but the radius R eventually decreases as the droplets populate the whole area. Then, as a consequence of the increase of the total volume with time, the fluid overflows (here, at 62 seconds). This removes all the emulsion droplets packed on the interface which overflows, and one then recovers the initial spreading radius R, as there are finally no more boundaries to pack the emulsion droplets [Fig. 3(b)].

It is important to point out that the accumulation of the emulsion droplets at the interface (inherent of a finite area A) has a timescale a few orders of magnitude smaller than the accumulation of the soluble surfactant in bulk (inherent of a finite volume V). This results from the fact that the surfactant solution flow rates are on the order of micromole/s, while the volume of the liquid pool is in liters.

To be complete regarding time evolution and finite size effects, we also wondered about the impact of the accumulation of the oil droplets on the surface tension outside the spreading distance (for radius and length bigger than R and L). We measured by a Wilhelmy plate technique (from Nima) the surface pressure as a function of time, $\Pi = \gamma_0 - \gamma$, outside of the spreading zone. Here, γ_0 is the interfacial tension of the initial solution (pure water), and γ is the surface tension at time t. It turns out that Π increases with time. However, performing the same experiment without the oil droplets shows that this interfacial pressure increase is recovered, and is therefore not due to the accumulation of droplets. We have identified the source of this increase to be the accumulation of insoluble impurities at the interfaces. Such molecules are always present at uncontrolled concentrations in our surfactant solutions. To investigate their effects, rather than trying to remove them with consecutive purifications, we have chosen to add controlled amounts of an insoluble species to an SDS solution. Myristic acid is then solubilized within the SDS micelles under heating. In Fig. 4, we report how the surface pressure, outside of the spreading zone, increases for different areas A and three myristic acid concentrations.

A first outcome is that these results are self-consistent, if one considers only the insoluble species. There are direct

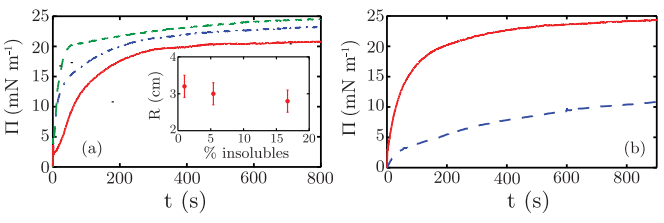

FIG. 4. (a) Interfacial pressure Π outside of the spreading zone as a function of time; solid line: 1% of myristic acid; dashed-dotted line: 5.4% of myristic acid; dashed line: 16.7% of myristic acid. Inset: steady-state radii, R, taken at $t = 30$ s, for the three different myristic acid concentrations. (b) Interfacial pressure Π outside of the spreading zone as a function of time; solid line: $S = 1600$ cm^2; dashed line: $S = 5400$ cm^2.

correlations between available areas, concentration, and pressure increase for these insoluble molecules. For instance, if the solution contains more insoluble species, or if the area A is smaller, pressure increases sooner. In other words, we can understand and control the rate of increase of the pressure outside the spreading zone, and this is fully explained in terms of accumulation of impurities at the interface.

In parallel, the second and crucial outcome of these tests is that there are no correlations between the dynamics of pressure increase and the dynamics of the spreading, evidenced by the tracers and shown in Fig. 3(a). The fact that the impurities accumulate slowly or rapidly can never be assigned to the evolution of $R(t)$; the timescales associated with $R(t)$ and $\Pi(t)$ are independent and uncorrelated. Indeed, the radius of the spreading zone stabilizes to its steady value well before the outside pressure tends to saturate. The beginning of the steady regime thus coincides with outside pressures which are either low or high (depending on the trough area A or of the amount of impurities), but still evolving. Moreover, as shown in the insert of Fig. 4(a), the value of this spreading radius R during the steady state (typically after 30 s of deposition) appears to be independent of the amount of myristic acid and thus of the surface tension of the reservoir fluid; we will come back on this effect of the surface tension difference in Sec. IV.

In other words, the insoluble species spread and populate the available area, independently of the finite spreading of the soluble ones. Though insoluble surfactants gradually change the outside surface tension, they are not responsible of a finite spreading of the soluble ones, nor of the steady-state value and time evolution of $R(t)$.

Thus, at this stage, we have shown that, if tracer packing is prevented and as long as velocities are high enough to detect sharp flow boundaries, clean and reliable steady values for R, L, and $V_{\max}$ are obtained. Moreover, the (un)controlled codeposition of insoluble impurities has no impact, as it is uncorrelated to the spreading of the soluble species.

III. THEORY

The scaling laws governing the interfacial and bulk flows, as well as the surfactant diffusion, have been established in [53]. The spreading area of the surfactants can be seen as an exchange zone between the interface and the bulk. In steady state, the incoming flux of surfactant Q deposited at the interface is entirely transferred to the bulk through this exchange zone, whose area thus adjusts to ensure this mass balance. The coupling between the hydrodynamics flow and the surfactant transfer from the interface to the bulk has two origins: (i) the surface tension gradient at the interface induces a Marangoni flow which spreads the surfactants and thus increases the area of the exchange zone; (ii) the flow washes the subphase and enhances the vertical concentration gradient, thus leading to a more efficient diffusion process. Quantifying this second point requires us to consider in detail the viscous and mass boundary layers that develop under the spreading zone. In this section, we rigorously derive the equations of motion, and prove that the concentration and velocity fields are both given by a master curve, once properly rescaled. This confirms that the qualitative scaling analysis made in [53] leads to the correct dependence for the characteristic velocity and for the spreading zone size.

A. Governing equations

The equations of motion are written in the axisymmetric situation, in cylindrical coordinates (r,ϕ,z). The origin of the cylindrical coordinates is the injection point and the interface is the plane $z=0$. The longitudinal case will be recovered with the same set of equations, in the limit $r\to\infty$ and with an injection point at a distance x_0 from the origin, as discussed at the end of the section. The fluid velocity is $\mathbf{v}=u(r,z)\mathbf{e_r}+v(r,z)\mathbf{e_z}$, the pressure $p(r,z)$, the bulk surfactant concentration $c(r,z)$, the interfacial surfactant concentration $\Gamma(r)$, and the surface tension $\gamma(r)$. The fluid's density is ρ and its viscosity η, the surfactant diffusion coefficient is D, and the gravity is g.

The Navier Stokes equation in cylindrical geometry is, projected on $\mathbf{e_r}$ and $\mathbf{e_z}$,

$$\rho\left(\frac{\partial u}{\partial t}+u\frac{\partial u}{\partial r}+v\frac{\partial u}{\partial z}\right) = -\frac{\partial p}{\partial r}+\eta\left(\frac{\partial^2 u}{\partial r^2}+\frac{1}{r}\frac{\partial u}{\partial r}-\frac{u}{r^2}+\frac{\partial^2 u}{\partial z^2}\right), \quad (1)$$

$$\rho\left(\frac{\partial v}{\partial t}+u\frac{\partial v}{\partial r}+v\frac{\partial v}{\partial z}\right) = -\frac{\partial p}{\partial z}-\rho g+\eta\left(\frac{\partial^2 v}{\partial r^2}+\frac{1}{r}\frac{\partial v}{\partial r}-\frac{v}{r^2}+\frac{\partial^2 v}{\partial z^2}\right), \quad (2)$$

and the fluid mass conservation is

$$\frac{\partial u}{\partial r}+\frac{u}{r}+\frac{\partial v}{\partial z}=0. \quad (3)$$

The velocity vanishes for $z\to-\infty$ and for $r\to\infty$. At the interface, the tangential stress conservation imposes

$$\eta\left(\frac{\partial u}{\partial z}+\frac{\partial v}{\partial r}\right)=\frac{\partial\gamma}{\partial r}. \quad (4)$$

This last relation is at the origin of the Marangoni flow.

In this study we assume that the surfactant exchange at the interface is limited by the bulk diffusion. The interface is thus at equilibrium with the subphase and $\Gamma(r)=\Gamma_{eq}(c(r,0))$. Moreover, the surface tension is assumed to be equal to the equilibrium surface tension $\gamma(r)=\gamma_{eq}(c(r,0))$. The master curve is only obtained using the linear approximation $\Gamma(r)=\partial_c\Gamma\, c(r,0)$ and $\gamma(r)=\gamma_0-|\partial_c\gamma|\, c(r,0)$, with $\partial_c\Gamma$ and $\partial_c\gamma$ two constants.

The convection diffusion equation for the surfactants is

$$\frac{\partial c}{\partial t}+u\frac{\partial c}{\partial r}+v\frac{\partial c}{\partial z}=D\left(\frac{\partial^2 c}{\partial r^2}+\frac{1}{r}\frac{\partial c}{\partial r}+\frac{c}{r^2}+\frac{\partial^2 c}{\partial z^2}\right), \quad (5)$$

and the surfactant mass conservation at the interface $z=0$ is

$$\frac{\partial\Gamma}{\partial t}+\frac{1}{r}\frac{\partial}{\partial r}(ru\Gamma)=-D\frac{\partial c}{\partial z}. \quad (6)$$

The set of bulk equations (1), (2), (3), and (5) involves the four unknown functions u, v, p, and c. It is closed with the boundary conditions $u=v=c=0$ for $z\to-\infty$ or $r\to\infty$ and with an hydrostatic value of p at these boundaries. At the interface $z=0$, we impose the conditions $v=0$ and $p=0$, and for u and c Eqs. (4) and (6).

This complex nonlinear system is identical to the one solved by Bratukhin *et al.* [57] for thermal Marangoni effects around a local heat source. The analytical solution of [57] corresponds to a true steady state in an infinite domain. In contrast, what we call steady state in the following is, strictly speaking, a quasi-steady state. Indeed the surfactants are continuously accumulating in the bulk, as discussed in Sec. II D. The far-field diffusion in the whole volume of the bucket is thus transient, whereas the local dynamics close to the interface is steady. The boundary conditions are thus modified in comparison with [57], as the fluid outside the mass boundary layer acts as a sink. In that case, the system can only be solved numerically, which is not the aim of the paper. Instead, using some well controlled approximations and the assumption of local steady state, it will be turned into an equivalent system with properly rescaled quantities, involving no physical parameters.

The unique solution of this dimensionless system will be the expected master curve. Coming back to the scaled physical quantities will provide the scaling laws for the velocity and the concentration fields and consequently the scaling laws for R (or L) and $V_{\max}$.

B. Existence of a master curve

The main approximation of our analysis is that the vertical length scales are much smaller than the horizontal ones. This is the usual basis of the boundary layer theory. Equations (1), (2), and (3) are rescaled with the following physical units: we define $r = XR_0$, $u = UU_0$, $z = \ell_v Z_1$ or $z = \ell_c Z_2$, $v = (\ell_v/R_0)U_0 V$, and $c = Cc^*$. The two vertical characteristic lengths are $\ell_v = \sqrt{\eta R_0/(\rho U_0)}$ for the viscous boundary layer and $\ell_c = \sqrt{R_0 D/U_0}$ for the mass boundary layer. At this point, the parameters R_0 and U_0 are arbitrarily chosen and must only satisfy $\ell_c \ll \ell_v \ll R_0$, a condition that will be checked *a posteriori*. The concentration c^* is $c(0,0)$ [or $c(x_0,0)$ for the linear case].

In steady state, Eqs. (1) and (3) become, using $\ell_v \ll R$,

$$U\frac{\partial U}{\partial X} + V\frac{\partial U}{\partial Z_1} = \frac{\partial^2 U}{\partial Z_1^2}, \tag{7}$$

$$\frac{\partial U}{\partial X} + \frac{U}{X} + \frac{\partial V}{\partial Z_1} = 0. \tag{8}$$

In this approximation, the pressure is hydrostatic in the whole domain, as deduced from Eq. (2), and thus does not depend on r.

The boundary equation at the interface is, from Eq. (4),

$$\frac{\partial U}{\partial Z_1} + \frac{\partial C_s}{\partial X} = 0 \quad \text{and} \quad V = 0, \tag{9}$$

with $C_s(X) = C(X,0)$ and with the velocity unit chosen as

$$U_0 = |\partial_c\gamma|\ell_v c^*/(\eta R_0). \tag{10}$$

Equations (9) are the interfacial boundary conditions for Eqs. (7) and (8) and show the first coupling between the flow and the surfactant transport, as discussed in the introduction of Sec. III.

A first-order expansion of V in the vertical coordinates Z_1 leads to $V(Z_1,X) = V(0,X) + Z_1\frac{\partial V}{\partial Z_1}(0,X)$. Using the boundary condition $V(0,X) = 0$ and the mass conservation Eq. (8) we obtain, for $Z_1 \ll 1$:

$$V(Z_1,X) = -\frac{Z_1}{X}\frac{\partial}{\partial X}(XU_s) \quad \text{with } U_s = U(0,X). \tag{11}$$

The rescaling of the surfactant transport, Eq. (5), is made with the second vertical length scale Z_2:

$$U\frac{\partial C}{\partial X} + \frac{\ell_v}{\ell_c}V\frac{\partial C}{\partial Z_2} = \frac{\partial^2 C}{\partial Z_2^2}. \tag{12}$$

For Z_2 of order unity, we get $Z_1 = \ell_c/\ell_v Z_2 \ll 1$. We thus can use the expansion (11) to obtain, at leading order in ℓ_c/ℓ_v,

$$U_s\frac{\partial C}{\partial X} - \frac{Z_2}{X}\frac{\partial}{\partial X}(XU_s)\frac{\partial C}{\partial Z_2} = \frac{\partial^2 C}{\partial Z_2^2}. \tag{13}$$

The interfacial boundary condition is, from (6),

$$\frac{1}{X}\frac{\partial}{\partial X}(XU_sC) + \frac{\partial C}{\partial Z_2} = 0 \quad \text{and} \quad C(0,0) = 1, \tag{14}$$

where the value of R_0 has been set to

$$R_0 = \partial_c\Gamma U_0\ell_c/D. \tag{15}$$

Combined with Eq. (10), this last equation allows to express the searched physical units U_0 and R_0 as power laws of well defined physicals quantities:

$$U_0 = (|\partial_c\gamma|c^*)^{1/2}\eta^{1/4}D^{1/4}\rho^{-1/2}\partial_c\Gamma^{-1/2}, \tag{16}$$

$$R_0 = (|\partial_c\gamma|c^*)^{1/2}\eta^{1/4}D^{-3/4}\rho^{-1/2}\partial_c\Gamma^{3/2}. \tag{17}$$

The transport equations (13) and (14) involve the interfacial velocity U_s, which reflects the second coupling between flow and surfactant transport.

Finally, we get two subsets of equations without any remaining physical nondimensional number: U and V are governed by Eqs. (7) and (8), with the variables (X,Z_1) and the boundary condition at interface Eq. (9) and C is governed by Eq. (13) with the variables (X,Z_2) and the boundary condition at interface Eq. (14).

These two subsystems are coupled but the coupling only involves the interfacial values $U_s(X)$ and $C_s(X)$. This allows to use the different variables Z_1 and Z_2 to solve each subsystem, without specifying the ratio Z_2/Z_1. The solution, denoted $(\hat{U},\hat{V},\hat{C})$, is thus unique and independent of any physical parameters. In principle, the self-consistency of the approach requires to check that $\hat{C}(X,Z_2)$ varies over a vertical distance of the order of unity, so that the expansion leading to Eq. (11) is justified.

The equations for the linear case are obtained by taking the limit $X \to \infty$ in all bulk and interfacial equations. The injection condition $C(0,0) = 1$ becomes $C(X_0,0) = 1$, with $X_0 \gg 1$ an arbitrary constant. Another set of solutions $(\tilde{U},\tilde{V},\tilde{C})$ is obtained for the linear case.

C. Predictions for the physical quantities

First, the total flux of surfactant Q is introduced in the problem, and replaces the interfacial concentration which is not measured experimentally. For the axisymmetric case, the

relation (6), once integrated over the whole interface, leads to

$$\begin{aligned} Q &= D\int_0^{2\pi}\int_0^{\infty}\frac{\partial c}{\partial z} r\,dr\,d\theta \\ &= -\int_0^{2\pi}\int_0^{\infty}\frac{1}{r}\frac{\partial}{\partial r}(r u_s \Gamma) r\,dr\,d\theta \\ &= 2\pi U_0 R_0 c^* \partial_c\Gamma \lim_{X\to 0} X U_s C\,. \end{aligned} \tag{18}$$

This leads to the relation

$$\partial_c\Gamma = K_a \frac{Q}{R_0 U_0 c^*} \tag{19}$$

with $K_a = (2\pi \lim_{X\to 0} X\hat{U}_s\hat{C})^{-1}$ a number.

This last point differs in the two geometries. In linear geometry we need to integrate between the injection line at $x_0 = R_0 X_0$ and $+\infty$ and we get

$$\partial_c\Gamma = K_l \frac{Q^{lin}}{c^* U_0} \tag{20}$$

with $Q^l = Q/(2\pi x_0)$ the flux per unit length and $K_l = 1/[\tilde{U}_s(X_0)\tilde{C}(X_0)]$.

The surface tension difference between the injection point, where $c = c^*$, and the pure water is denoted below by $\Delta\gamma = |\partial_c\gamma|c^*$. The expression (19) [or (20) for the linear case] is substituted in Eqs. (16) and (17), and the system obtained is solved to get a new explicit expression for U_0 and R_0.

For the axisymmetric case,

$$R_0^a = K_a^{\frac{3}{4}}\left(\frac{Q}{c^*}\right)^{\frac{3}{4}}\left(\frac{\eta\rho}{\Delta\gamma^2 D^3}\right)^{\frac{1}{8}}, \tag{21}$$

$$U_0^a = K_a^{-\frac{1}{4}}\left(\frac{c^*\Delta\gamma^3}{Q}\right)^{\frac{1}{4}}\left(\frac{D}{(\eta\rho)^3}\right)^{\frac{1}{8}}, \tag{22}$$

and, for the longitudinal case,

$$R_0^l = K_l^3\left(\frac{Q^l}{c^*}\right)^3\sqrt{\frac{\eta\rho}{\Delta\gamma^2 D^3}}, \tag{23}$$

$$U_0^l = K_l^{-1}\frac{c^*\Delta\gamma}{Q^l}\sqrt{\frac{D}{\eta\rho}}. \tag{24}$$

Note that, for comparison with the experimental results in the linear configuration, we use $Q^l = Q/H$ to obtain the flux per unit length Q^l.

All the physical quantities can be deduced from the solution $(\hat{U}, \hat{V}, \hat{C})$ or $(\tilde{U}, \tilde{V}, \tilde{C})$ and the physical units. The spreading distance R in the axisymmetric configuration can be defined as the radius at which the velocity is a small fraction ϵ of the maximal velocity U_m; it is thus given by $R = R_0^a X_s$ with X_s verifying $\hat{U}(X_s) = \epsilon\hat{U}_{\max}$; the maximal physical velocity is $V_{\max} = U_0^a\hat{U}_{\max}$. Similarly, in the linear configuration, L and $V_{\max}$ are proportional to R_0^l and U_0^l.

These predictions are compared to experimental results in Sec. IV. As the solutions of the rescaled systems are not known, only the functional dependencies can be tested. We thus defined R_{th}, L_{th}, V_{th}^a, and V_{th}^l from R_0^a, R_0^l, U_0^a, and U_0^l by omitting the unknown numerical prefactors.

D. Validation of the approximations

The comparison with the experimental results discussed in Sec. IV shows that the master curves $(\hat{U}, \hat{V}, \hat{C})$ and $(\tilde{U}, \tilde{V}, \tilde{C})$ and their derivatives are of order 1 in the whole domain, as expected from the governing equations. Consequently, R and R_0 are of the same order of magnitude, as well as U_0 and $V_{\max}$. The assumption $\ell_c \ll \ell_v \ll R_0$ can thus be checked using the experimental measurement. With $R \sim 10^{-2}$m, $\eta \sim 10^{-3}$ Pa s, $\rho \sim 10^3$ kg m^{-3}, $V_{\max} \sim 10^{-1}$ m s^{-1}, and $D \sim 10^{-10}$ m^2 s^{-1}, we get $\ell_v \sim 3\times 10^{-4}$ m and $\ell_c \sim 3\times 10^{-6}$ m, thus validating the scale separation used to establish the master curve.

The steady state is also a crucial assumption, which requires a discussion. The plateau duration τ_p can be bigger than hundreds of seconds. In the Navier-Stokes equation, $\rho\partial u/\partial t$ is at most of the order of $\rho U_0/\tau_p \sim 1$, whereas $\eta\partial^2 u/\partial z^2 \sim \eta U_0/\ell^2 \sim 10^3$. A similar result is obtained for the transport equation. For the two equations, the validity of the steady state assumption arises from the fact that the intrinsic time scale $R_0/U_0 \sim 0.1$ s is much smaller than the experimental time scales.

Lastly, note that all the parameters involved in the scaling laws (21)–(24) are control parameters or well defined physical properties, excepted for c^* which is the concentration of the subphase at the injection point. Our previous experiments showed that, for anionic surfactants, if one assigns the cmc value to c^*, one gets consistent results and the theoretical scaling is recovered for the spreading distance [53]. We will return below, with new experimental results and interpretation, to this relation between $c*$ and the cmc for surfactants.

IV. RESULTS AND COMPARISONS TO THE MODEL

A. Axisymmetric spreading

As already explained, we focus here on two macroscopic quantities, which are the spreading distance (here, the radius R), and the maximal velocity $V_{\max}$ within the spreading area. Figures 5 and 6 summarize how these quantities depend on the various experimental parameters.

In Fig. 5(a), the role of the influx rate Q is shown. We first need to figure out if the key parameter is really the number of surfactant molecules deposited per second, so that μmol s^{-1} is the correct dimension for Q. In practice, the flow rate Q, expressed in μmol s^{-1}, is $Q = Q_v c_e$, where Q_v is the volumetric flow rate delivered by the syringe (ml s^{-1}) and c_e is the concentration of surfactant in the emulsion. As the emulsion contains 50% oil, this concentration c_e is half of the initial concentration in the water phase.

To solve this issue, in Fig. 5(a), we show data obtained by the two approaches: keeping Q_v constant and changing c_e, or the opposite. The results show that it is equivalent to varying Q by one or the other way. The fact that the relevant quantity is expressed in μmol s^{-1} also demonstrates that all the surfactants are involved, not only the free monomers (whose concentration saturates at the cmc). Even surfactants initially within micelles are indeed engaged in the spreading process; this is not a trivial result, as the ability for micelles to rapidly disassemble to get involved in interfacial dynamical processes is complex and not fully understood [58]. In terms of data fitting, the solid line in Fig. 5(a) is a power law with an exponent 3/4, in

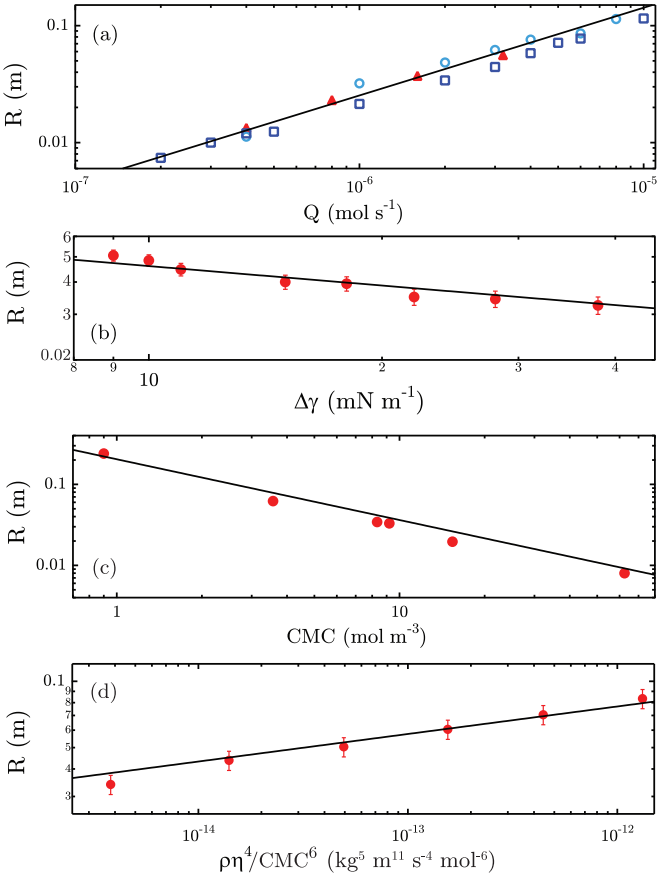

FIG. 5. (a) Variation of the radius R with the influx rate Q in μmol/s. Squares: 50%-50% oil-in-water emulsion at a fixed concentration of SDS (15 cmc); circles: 50%-50% oil-in-water emulsion with an influx rate of 1 ml/min varying concentration of the SDS solution; triangles: foam with a liquid fraction of 20%. (b) Variation of the radius R with the difference of surface tension, $\Delta\gamma$; $Q = 1\ \mu\text{mol s}^{-1}$. (c) Variation of radius R with surfactant cmc, $Q = 1\ \mu\text{mol s}^{-1}$. (d) Variation of the radius R when glycerol is added, modifying both density, viscosity, and cmc; $Q = 1\ \mu\text{mol s}^{-1}$. In the four graphs, solid lines correspond to the predicted scaling laws; exponents are respectively 3/4, $-1/4$, $-3/4$, and $1/8$ for (a) to (d).

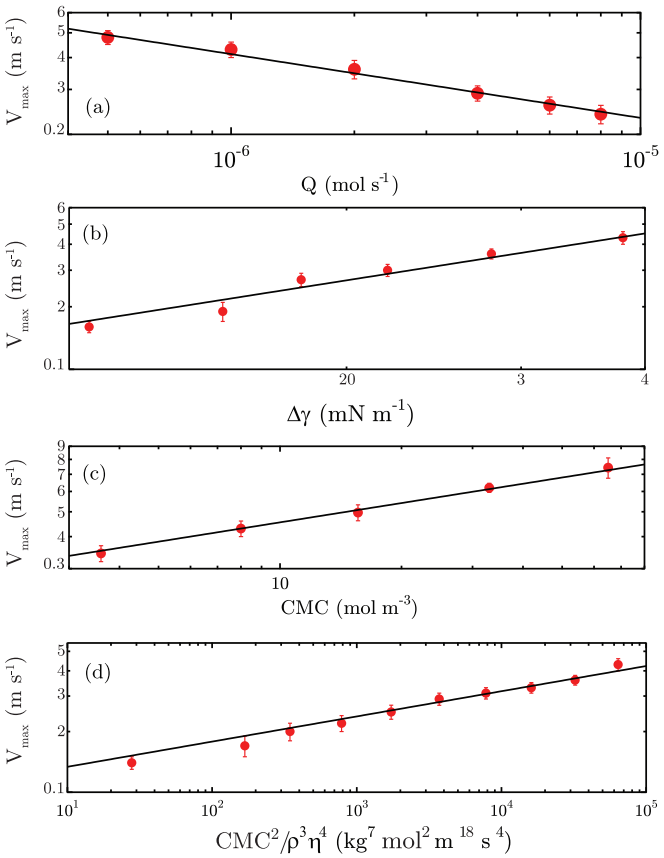

FIG. 6. (a) Variation of the maximum velocity V_{max} with the influx rate. (b) Variation of the maximum velocity V_{max} with $\Delta\gamma$, $Q = 1\ \mu\text{mol s}^{-1}$. (c) Variation of the maximum velocity V_{max} with cmc, $Q = 1\ \mu\text{mol s}^{-1}$. (d) Variation of the maximum velocity V_{max} when glycerol is added, $Q = 1\ \mu\text{mol s}^{-1}$. In the four graphs, solid lines correspond to the predicted power laws; exponents are respectively $-1/4$, 3/4, 1/4, and 1/8 for (a) to (d).

good agreement with Eq. (21). Note also that we plot the data obtained with using bubbles as tracers, demonstrating that tracers have no effect on R, for any Q. Regarding the effect of Q on the flow velocity, Fig. 6(a) shows that the velocity decreases with an increase of Q. Though it seems counterintuitive, this is in agreement with our model, and the data can be well adjusted with the expected power law of exponent 1/4 given by Eq. (22).

In Fig. 5(b), we present the results on the effect of the initial gradient of surface tension. In practice, the deposited solution is always at the lowest value of the surface tension (as the concentration is above the cmc) and we tune the gradient by initially adding the same surfactant in the bulk water layer. In the axisymmetric configuration, the spreading radius is expected to scale as $R \sim \Delta\gamma^{-1/4}$. Indeed, we find data consistent with such an exponent, although the accuracy is not optimal as the range of variation remains low. This is measured for a given Q, but it remains true at other values. As well, a scaling regime is found for velocity, which can be well adjusted by a power law of exponent 3/4, in agreement with Eq. (22) [Fig. 6(b)].

We can make here a few important remarks. First, note the counterintuitive behavior with $\Delta\gamma$; the fact that the radius R increases with decreasing $\Delta\gamma$ is not a straightforward behavior. Second, when reducing $\Delta\gamma$, we get to the experimental limitation in terms of velocity, discussed previously. As we approach an initial concentration of cmc/2 in the bulk, V_{max} decreases down to values so low, $V_{max} \approx 0.15$ m s^{-1}, that the boundaries of the spreading zone are difficult to localize, thus preventing reliable measurement of R. Therefore, we cannot have access to $\Delta\gamma$ typically lower than 10 mN/m. Note finally that the low dependance of R with the surface tension gradients, $R \sim \Delta\gamma^{-1/4}$, is consistent with the tests with insoluble myristic acid, explaining why the accumulation of myristic acid was decreasing the surface tension, without significant changes of R.

Further experiments deal with the role of surfactant amphiphilicity; in the model, a typical concentration c^* arises as the relevant scale to link the flow properties to the molecule properties. We can compare our data to this model, considering that, for surfactants, c^* is the cmc. The graph in Fig. 5(c) shows

that the spreading distances for different types of surfactants can actually be compiled in a consistent manner when plotted as a function of the surfactant cmc (the solid line is a power law with an exponent 3/4, as predicted). This is supplementing our previous results [53], by also showing that nonionic molecules behave similarly. Moreover, we demonstrate the relevant role of the cmc also in the scaling of the flow velocity [Fig. 6(c)]: we find that, for all the surfactants, $V_{\max}$ scales with $\mathrm{cmc}^{1/4}$, in agreement with Eq. (22).

Let us comment on this equality between c^* and the cmc. Indeed, the details of the flow and transport properties close to the injection point, leading to this equality, are not entirely elucidated. We propose the following scenario. Three-dimensional mixing occurs close to the injection point, leading to a small volume of radius r_s at a concentration of intermediate value between the injected concentration (larger than the cmc) and the cmc. This region corresponds to the white dense region seen in Fig. 2 close to the injector. At the interface, the boundary of this region, of typical radius r_s, saturates at its maximal concentration, and the Marangoni stress is thus vanishing for $r < r_s$. For $r > r_s$, the subphase concentration gets below the cmc, allowing for concentration gradients at the interface, and Marangoni flows. Our model only describes what happens for $r > r_s$. It is difficult to estimate this radius theoretically, but experimentally the velocity profile shows a sharp increase at a distance r_s, significantly larger than the injector size. However, as $r_s \ll R$, the assumption of a point source with a local subphase concentration equal to the cmc is valid.

Finally, we have also investigated the dependence with the fluid viscosity. This is a bit more complex than the other parameters, as our approach based on the addition of glycerol changes not only the viscosity, but also the diffusion coefficient, the density, and (more slightly) the cmc [59,60]. If we assume that $D \sim 1/\eta$, and group the terms of Eq. (21) impacted by the glycerol, we get that R should scale like $R \sim (\rho\eta^4\,\mathrm{cmc}^{-6})^{1/8}$, with all other quantities kept constant. We tested this combination in Fig. 5(d), plotting the data obtained as glycerol is added, and get good agreement (the solid line is a power law with an exponent 1/8). The same multiple effect of glycerol is also found for the velocity: the glycerol-dependent combination is $V_{\max} \sim (\rho^{-3}\,\eta^{-4}\,\mathrm{cmc}^2)^{1/8}$. The data are given in Fig. 6(d), and once again they can be fitted by the expected power law.

We would like to conclude this part with two remarks. First, we are again limited in this study on viscosity by too low velocities at high concentration of glycerol; increasing the bulk viscosity reduces the velocity, leading to smooth and flat velocity profiles which then cannot be optically detected. The threshold speed is here again of the order of $V_{\max} \approx 0.15\,\mathrm{m\,s^{-1}}$. Second, if only glycerol is added in the deposited solution and not in the water pool, one gets the same results as without glycerol. In fact, glycerol is not mandatory in the injection fluid, as long as it is added in the pool. To vary the surfactant spreading flow through viscosity, it is just sufficient to only change the viscosity of the liquid reservoir.

B. Longitudinal spreading

In this second geometrical configuration, as shown in Eq. (23), the predicted power-law exponents for L are larger than those predicted for the axisymmetric case for R, hence they are *a priori* easier to check experimentally.

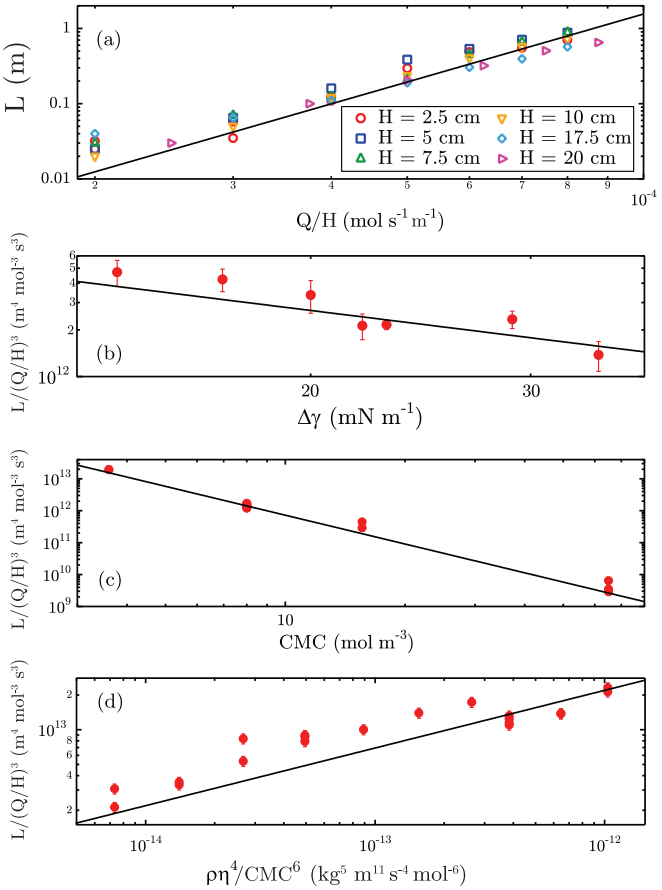

FIG. 7. (a) Variation of the length L with Q/H. (b) Variation of the length L, renormalized by influx and gap thickness, with the surface tension difference $\Delta\gamma$. (c) Variation of the length L, renormalized by influx and gap thickness, with the surfactant cmc. (d) Variation of the length, renormalized by influx and gap thickness, when glycerol is added. In the four graphs, solid lines correspond to the predicted scaling laws; exponents are respectively 3, −1, −3, and 1/2 for (a) to (d).

Nonetheless, this increase in the value of the exponents introduces experimental limitations due to the large variations of L and $V_{\max}$ with the experimental parameters. Despite our 2-m-long trough, the range for L remains finite. Moreover, we also need to keep the width of the channel H much smaller than L to remain in a longitudinal spreading condition. We solve this issue by taking advantage of the fact that data for L is predicted to be rescalable by $(Q/H)^3$. This first requires us to check these dependencies with Q and H, so that the other data can subsequently be normalized by these quantities. In Fig. 7(a), data for different Q and H are compiled. It turns out that the different sets of data, at various H, can be collapsed on a single curve, once plotted as a function of Q/H. As well, the solid line corresponds to a power law with an exponent 3, in agreement with Eq. (23). Corresponding velocity data are plotted in Fig. 8(a). The velocity decreases with Q and the data can be adjusted by a power law of exponent −1 in agreement with Eq. (24). From now on, all data regarding L will be rescaled by Q/H.

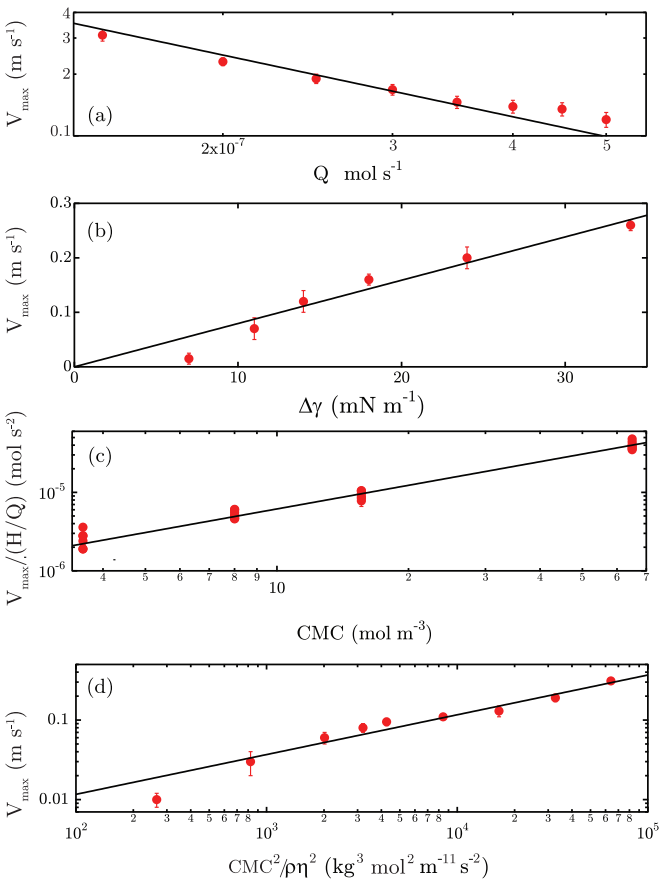

FIG. 8. (a) Variation of the maximum velocity V_{max} with the influx rate. (b) Variation of the maximum velocity V_{max} with $\Delta\gamma$, $Q = 1$ μmol s^{-1}. (c) Variation of the maximum velocity V_{max}, normalized by influx and gap thickness, with cmc. (d) Variation of the maximum velocity V_{max} when glycerol is added. In the four graphs, solid lines correspond to the predicted scaling laws; exponents are respectively -1, 1, 1, and 1/2 for (a) to (d).

Concerning the effect of the difference of surface tension $\Delta\gamma$, data and power-law adjustments are given in Figs. 7(b) and 8(b) for L and V_{max}. As explained before, L is first rescaled by Q/H to keep experimentally convenient values for L. This is not necessary for V_{max}, as its dependence is smaller with $\Delta\gamma$, so that experiments can be done at any single H. Again, the experimental behaviors correspond well to Eqs. (23) and (24): we get $L \sim \Delta\gamma^{-1}$ and $V_{max} \sim \Delta\gamma$. Note that this confirms the nontrivial increase of the spreading distance as $\Delta\gamma$ is reduced, as also found in the axisymmetric configuration. The study at small $\Delta\gamma$ is here again prevented, as it corresponds to too low values of V_{max}, so that we could not detect L accurately. Note also that, in Fig. 8(b), all the data do not correctly match with the scaling law. The smallest values of V_{max} fall below the fitting curve; it is possible that, in these experimental conditions providing low interfacial speeds, some of the approximations start to be no longer valid, or that the spreading distance is not long enough to obtain a fully developed velocity profile (with the correct maximal velocity).

For the effect of the surfactant amphiphilicity, results are given in Figs. 7(c) and 8(c) for L and V_{max}. Once again, a good agreement with the model is found once data are plotted as a function of the cmc: the solid lines in these graphs are respectively power laws with exponents -3 and 1. The nonionic surfactants here again show the same behavior as the ionic ones.

Finally, glycerol is also added to our bulk solutions. As explained previously, it changes the bulk viscosity, the cmc, the density, and the diffusion coefficient. In this longitudinal geometry, once we group these effects, we get $L \sim (\rho\eta^4/\mathrm{cmc}^6)^{1/2}$. Measurements of L are plotted as function of this combination in Fig. 7(d), and can be well fitted by the predicted exponent. The impact of glycerol on the velocity is also successfully checked in Fig. 8(d) in that case, the scaling $V_{max} \sim (\rho^{-1}\eta^{-2}\,\mathrm{cmc}^2)^{1/2}$ groups the different effects of the added glycerol. Note that, as for the effect of the surface tension difference, smallest values of V_{max} appear to be slightly too low when compared to the rest of the data, probably evidencing some limits of the validity of our model.

C. Data collapsing

Another way to compare the data to the model consists of plotting the different experimental quantities as a function of the predicted ones. This is shown in Fig. 9 for the distances R and L and the associated velocities V_{max}. The important point here is that this approach, by collapsing the effect of *all* the parameters on a single graph, is much more stringent than the comparisons made separately for each parameter. It turns out that, for both geometrical configurations and for all the measured quantities, these plots reveal no inconsistency between the parameters. All the data collapse rather well; such an agreement confirms, as a whole, the existence of a master curve for the velocity field, both in axisymmetric and longitudinal geometries. Moreover, this provides also quantitative information on the prefactor relating the spreading distances and the maximal velocities to the length and velocity units. From the graphs of Fig. 9, the experimental prefactors are respectively 0.39, 1.45, 0.1, and 1.7 for the panels (a) to (d). Except for the spreading distance in the longitudinal configuration which gives a prefactor of 0.1, the other prefactors remains close to unity, which validates the assumptions made in the model (see Sec. III D). Only a full quantitative analysis could provide derivations of the prefactors, and might explain the different values of the prefactors.

V. MARANGONI FLOWS AS A TOOL TO MEASURE cmc OF COMPLEX SOLUTIONS

Taking advantage of the cmc dependence of the spreading distance R or L, we tested our ability to derive how the cmc changes with solution components, from relative measurements of R.

The first test has been performed by adding salt to a surfactant solution, as it is known to decrease the cmc [4,61] without changing the other physicochemical properties of the solution. The spreading radius $R(c_s)$ has been measured for SDS solutions containing different amounts of added NaCl, at concentration c_s in the range 0–0.1 mol/l. From Eq. (21) we get the relation $\mathrm{cmc}(c_s)/\mathrm{cmc}(0) = [R(0)/R(c_s)]^{4/3}$.

In Fig. 10(a), we show the predicted variation of the cmc, normalized by the value for no salt, as a function of the salt concentration. We also add results from the literature, obtained

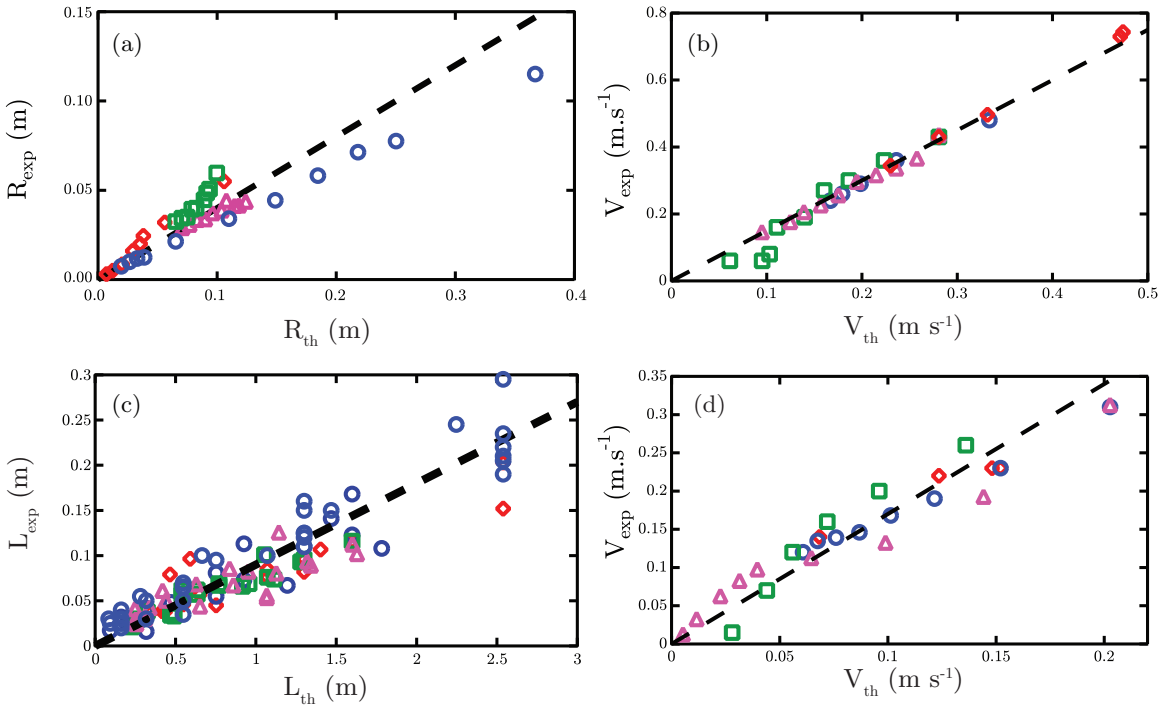

FIG. 9. (a) and (b) Experimental radius and velocity versus theoretical radius and velocity in axisymmetric configuration. (c) and (d) Experimental length and velocity versus theoretical length and velocity in longitudinal configuration. For the four graphs, circles: varying influx rate; triangles: glycerol effect via viscosity, density and cmc; squares: varying $\Delta\gamma$; diamonds: varying cmc.

by measuring the cmc with the pendant drop method [61], and we get an excellent agreement. Especially, our technique based on the optical determination of the cmc was able to reproduce the nonlinear behavior, with a faster decrease at low salt concentration than at higher c_s.

In another test, we mixed two surfactant solutions, C_{12}TAB and, at different ratios, and analyzed the cmc of the mixed solutions. Figure 10(b) shows how the normalized cmc evolves as a function of the ratio of mixing. For comparison, we add the data obtained by the pendant drop technique [62]. Once again, the agreement is excellent, here also being able to capture nonlinear behavior. This proves that the approach based on imaging the spreading distance can actually provide the evolution of a cmc as a function of the additives.

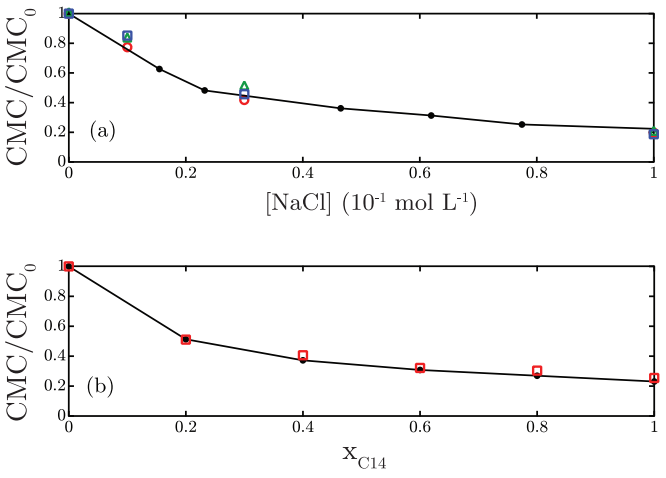

FIG. 10. (a) normalized cmc deduced from optical measurement of R and using our model as a function of the NaCl concentration added in a SDS solution. Circles: $Q = 0.3$ μmol s^{-1}; squares: $Q = 0.6$ μmol s^{-1}; triangles: $Q = 1.2$ μmol s^{-1}. Line: data collected by the pendant drop technique. (b)Normalized cmc deduced from optical measurement of R and using our model as a function of the molar fraction of C_{14}TAB in a solution of C_{12}TAB. Circles: our experiments; line: data collected by the pendant drop technique.

For comparison, one must remember that the pendant drop technique requires numerous dilutions, measurements of the surface tension γ for each concentration c, and detection of a kink in the $\gamma(c)$ curve. This protocol is actually much more time-consuming that our spreading-based method. Nevertheless, one must keep in mind that there are limitations in the range of accessible cmc (for practical reasons, R must remain within tens of cm).

VI. CONCLUSIONS AND PERSPECTIVES

We have reported new experimental results on soluble surfactant spreading, confirming and strongly supplementing those we reported earlier [53]. In particular, for two different geometrical configurations and for both the spreading distance and the spreading velocity, we have shown that all their variations with experimental parameters can be explained. Moreover, as tested in Fig. 9, the different dependences are self-consistent, and all the data can be rescaled and compiled on master curves. All together, this work proves that our model relies on good theoretical building blocks and assumptions.

We want to point out that some of these results are indeed striking. First of all, it was not obvious *a priori* that a steady-state solution, with finite R or L, necessarily exists for this problem of soluble surfactant spreading. Also, the

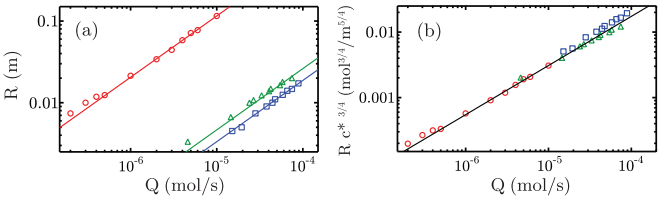

FIG. 11. (a) spreading radius as a function of the flow rate. Circles: SDS solution at 15 cmc; triangles and squares: data with alcohols from [38–41]. (b) Normalized spreading radius, using the cmc for the surfactant and the limit of solubility, c^s, for the alcohols.

various scaling exponents of Eqs. (21)–(24) are far from obvious, and cannot be derived by trivial scaling combinations. As an example, the dependencies with $\Delta\gamma$ or viscosity are clearly counterintuitive. Quantitatively, it also turns out that the unknown prefactors in the Eqs. (21)–(24) are of the order of 1.

These results bring some important insights both on fundamental and practical issues. Fundamentally speaking, we show that, by studying surfactants, a *finite* hydrophobicity goes with a *finite* equilibrium concentration (cmc) and with a *finite* distance over which gradients are dynamically relaxed. The equilibrium-defined cmc turns out to also be the scale for including the hydrophobicity in dynamical processes.

From a practical point of view, this work provides some strategies for new ways of rapid cmc measurement, especially well adapted to easily monitor how it evolves as a formulation is designed. Note also that, for all practical conditions, it becomes crucial to check first whether the typical characteristic dimension d of the tank is bigger or smaller than R (or L); in the case where $d < R$, soluble surfactants will behave as insoluble ones, meaning that finite-size effects dominate finite-hydrophobicity ones.

We also want to point out that we have investigated and understood here a rather "simple" spreading situation. At this stage, we believe that the ingredients of our model can be useful building blocks for a few other similar but more complex experiments (in particular those when evaporation and/or chemical reaction also compete with bulk diffusion [63,64], or when anisotropy comes into play to induce motion [18,19]).

As a first step towards a generalization of our analysis, oriented up to now towards surfactants and cmc, we have collected previous data on the spreading of some soluble alcohols. These molecules have no cmc, but a characteristic solubility concentration c^s, which is discussed in [38–41]. Usually, above the solubility limit, alcohols start to make large aggregates, much bigger than micelles, while there is no thermodynamical equilibrium such as the one between interfaces and micelles for surfactants. This is in fact closer to the case of surfactant aggregation below a Krafft temperature. In Fig. 11(a), we have replotted these data as a function of Q, together with our data for SDS. Then, in Fig. 11(b), we have compiled on the same graph the alcohol data, taking c^s for the typical concentration c^* in Eq. (21); it turns out that all these data, once normalized by the relevant scale for concentration, collapse on the single curve. This simple and successful test of rescaling different data sets—ours for surfactant associated to a cmc, and others taken in the literature for alcohols associated with a solubility concentration—clearly demonstrates the generic relevance of our work. Beyond this proof of concept, many issues are still pending to fully understand how far the Marangoni behavior of alcohols and the one of surfactants are similar. In particular one has to determine how the surface tension is modified by the alcohols, below and above the critical concentration c^*. Further progress on this issue is expected by studying a class of molecules, named solvo-surfactants [65], which exhibit properties both of solvents and of surfactants.

The study as a function of time has also brought some interesting features. Because of the finite area of the tank, we have shown that tracers and insoluble impurities accumulate with time. If the packing of the tracers is the main source for reducing the spreading zone with time, we have found that the spreading of insoluble and soluble turns out to be completely uncorrelated. Surprisingly, we show here that, in the context of Langmuir monolayers, it is possible to deposit a controlled amount of insoluble species on a free interface by dispersing them first into a water-soluble surfactant solution. This could be used as an alternative to the generally used nonpolar solvent.

So far, we have focused on the spreading distances, and associated velocities. Still, many aspects deserve some further work. First, it might be useful to get rid of any tracers, meaning that other means for measuring the flow boundaries need to be found. In fact, some preliminary results show that one can also get some insights by profilometric techniques [66]. This technique also gives us some information on the nonflat steady-state shape of the interface, opening interesting links with other types of dynamical deformations (such as the hydraulic bump [67]). A thorough description would also require the measurement of the radial surfactant concentration profiles, as well as velocity circulation in bulk. Those are various works in progress, which are beyond the scope of this article and will be published later. As well, further work is also required to discriminate between the various possible hydrodynamical instabilities to find out the origins of the complex recirculating flows located at the boundary of the spreading zone. Last, preliminary experiments of deposition of concentrated surfactant solution at the interface between water and oil reveal other striking features.

ACKNOWLEDGMENTS

The authors thank Rodrigo Leite Pinto for his help during experiments and Benjamin Dollet for discussions on the model. The authors also thank Howard A. Stone for stimulating discussions.

[1] C. Tanford, Science **200**, 1012 (1978).
[2] C. Tanford, *The Hydrophobic Effect: Formation of Micelles and Biological Membranes*, 2nd ed. (Wiley-Interscience, New York, 1980).
[3] D. Chandler, Nature (London) **437**, 640 (2005).
[4] M. J. Rosen, *Surfactants and Interfacial Phenomena*, 3rd ed. (Wiley-Interscience, Hoboken, NJ, 2004).
[5] J. Israelachvili, *Intermolecular and Surface Forces*, 3rd ed. (Academic Press, New York, 2011).
[6] C. H. Chang and E. I. Franses, Colloids Surf. A **100**, 1 (1995).

[7] P. Xun Li, R. K. Thomas, and J. Penfold, Langmuir **30**, 6739 (2014).
[8] L. Maibaum, A. R. Dinner, and D. Chandler, J. Phys. Chem. B **108**, 6778 (2004).
[9] C. Marangoni, Il Nuovo Cimento Series 2 **5-6**(1), 239 (1871).
[10] V. G. Levich and V. S. Krylov, Annu. Rev. Fluid Mech. **1**, 293 (1969).
[11] R. Karlsson *et al.*, Langmuir **18**, 4186 (2002).
[12] P. G. Dommersnes, O. Orwar, F. Brochard-Wyart, and J. F. Joanny, Europhys. Lett. **70**, 271 (2005).
[13] M. Staykova, D. P. Holmes, C. Read, and H. A. Stone, Proc. Natl. Acad. Sci. USA **108**, 9084 (2011).
[14] F. Leal-Calderon, V. Schmitt, and J. Bibette, *Emulsion Science: Basic Principles* (Springer, Berlin, 2007).
[15] I. Cantat, S. Cohen-Addad, F. Elias, R. Hohler, F. Graner, O. Pitos, F. Royer, and A. Saint-Jalmes, *Foams: Structure and Dynamics* (Oxford University Press, Oxford, UK, 2013).
[16] R. M. Harshey, Annu. Rev. Microbiol. **57**, 249 (2003).
[17] T. Eisner, M. Eisner, and M. Siegler, *Secret Weapons: Defense of Insects, Spiders, Scorpions, and Other Many- Legged Creatures* (Belknap-Harvard, Cambridge, MA, 2005).
[18] J. W. M. Bush and D. L. Hu, Annu. Rev. Fluid Mech. **38**, 339 (2006).
[19] E. Lauga and A. M. J. Davis, J. Fluid Mech. **705**, 120 (2012).
[20] A. H. Jobe, New Engl. J. Med. **328**, 861 (1993).
[21] J. B. Grotberg, Annu. Rev. Fluid Mech. **26**, 529 (1994).
[22] D. Quéré, Ann. Rev. Fluid Mech. **31**, 347 (1999).
[23] J. F. Hernandez-sanchez, A. Eddi, and J. H. Snoeijer, J. Fluid Mech. (to be published).
[24] G. T. Barnes, Agr. Water Manage. **95**, 339 (2008).
[25] M. A. Herzig, G. T. Barnes, and I. R. Gentle, J. Colloid Interface Sci. **357**, 239 (2011).
[26] C. J. W. Breward, R. C. Darton, P. D. Howell, and J. R. Ockendon, Chem. Eng. Sci. **56**, 2867 (2001).
[27] P. D. Howell and C. J. W. Breward, J. Fluid Mech. **29**, 275 (2003).
[28] C. D. Bain, Adv. Colloid Interface Sci. **144**, 4 (2008).
[29] D. P. Gaver and J. B. Grotberg, J. Fluid Mech. **213**, 127 (1990).
[30] D. P. Gaver and J. B. Grotberg, J. Fluid Mech. **235**, 399 (1992).
[31] O. E. Jensen and J. B. Grotberg, J. Fluid. Mech. **240**, 259 (1992).
[32] J. B. Grotberg and D. P. Gaver, J. Colloid Interface Sci. **178**, 377 (1996).
[33] O. K. Matar and S. M. Troian, Chaos **9**, 141 (1999).
[34] A. Chauhan, T. F. Svitova, and C. J. Radke, J. Colloid Interface Sci. **222**, 221 (2000).
[35] O. E. Jensen and S. Naire, J. Fluid. Mech. **554**, 5 (2006).
[36] O. K. Matar and R. V. Craster, Soft Matter **5**, 3801 (2009).
[37] S. L. Strickland, M. Hin, M. R. Sayanagi, C. Gaebler, K. E. Daniels, and R. Levy, Phys. Fluids **26**, 042109 (2014).
[38] D. G. Suciu, O. Smigelschi, and E. Ruckenstein, AIChE J. **13**, 1120 (1967).
[39] D. G. Suciu, O. Smigelschi, and E. Ruckenstein, AIChE J. **15**, 686 (1969).
[40] E. Ruckenstein, O. Smigelschi, and D. G. Suciu, Chem. Eng. Sci. **25**, 1249 (1970).
[41] D. G. Suciu, O. Smigelschi, and E. Ruckenstein, J. Colloid Interface Sci. **33**, 520 (1970).
[42] A. Mizev, Phys. Fluids **17**, 122107 (2005).
[43] A. Mizev, A. Trofimenko, D. Schwabe, and A. Viviani, Eur. Phys. J. Spec. Top. **219**, 89 (2013).
[44] D. Halpern and J. B. Grotberg, J. Fluid Mech. **237**, 1 (1992).
[45] O. E. Jensen and J. B. Grotberg, Phys. Fluids **5**, 58 (1993).
[46] Q. Wang, M. Siegel, and M. R. Booty, Phys. Fluids **26**, 052102 (2014).
[47] J. L. Bull and J. B. Grotberg, Exp. Fluids **34**, 1 (2003).
[48] K. S. Lee and V. M. Starov, J. Colloid Interface Sci. **314**, 631 (2007).
[49] K. S. Lee and V. M. Starov, J. Colloid Interface Sci. **329**, 361 (2009).
[50] S. M. Troian, X. L. Wu, and S. A. Safran, Phys. Rev. Lett. **62**, 1496 (1989).
[51] B. D. Edmonstone, R. V. Craster, and O. K. Matar, J. Fluid Mech. **564**, 105 (2006).
[52] M. Hanyak, D. K. N. Sinz, and A. A. Darhuber, Soft Matter **8**, 7660 (2012).
[53] M. Roché, Z. Li, I. M. Griffiths, S. LeRoux, I. Cantat, A. Saint-Jalmes, and H. A. Stone, Phys. Rev. Lett. **112**, 208302 (2014).
[54] V. Bergeron, Langmuir **13**, 3474 (1997).
[55] M. Yamanaka, T. Amano, N. Ikeda, M. Aratono, and K. Motomura, Colloid Polym. Sci. **270**, 682 (1992).
[56] M. T. Yatcilla, K. L. Herrington, L. L. Brasher, E. W. Kaler, S. Chiruvolu, and J. A. Zasadzinski, J. Phys. Chem. **100**, 5874 (1996).
[57] I. K. Bratukhin and L. N. Maurin, J. Appl. Math. Mech. USSR **31**, 605 (1967).
[58] Q. Song, A. Couzis, P. Somasundaran, and C. Maldarelli, Colloids Surf. A **282-283**, 162 (2006).
[59] G. D'Errico, D. Cicarelli, and O. Ortona, J. Colloid Interface Sci. **286**, 747 (2005).
[60] C. Carnero-Ruiz, L. Diaz-Lopez, and J. Aguiar, J. Colloid Interface Sci. **305**, 293 (2007).
[61] I. M. Umlong and K. Ismail, Colloids Surf. A **299**, 8 (2007).
[62] K. Holmberg *et al.*, *Surfactants and Polymers in Aqueous Solutions* (Wiley, New York, 2002).
[63] V. Pimienta, M. Brost, N. Kovalchuk, S. Bresch, and O. Steinbock, Angew. Chem. Int. Edit. **50**, 10728 (2011).
[64] N. M. Kovalchuk and D. Vollhardt, Adv. Colloid Interface Sci. **120**, 1 (2006).
[65] K. Lunkenheimer, S. Schroedle, and W. Kunz, Prog. Colloid Polym. Sci. **126**, 14 (2004).
[66] P. Cobelli, A. Maurel, V. Pagneux, and P. Petitjeans, Exp. Fluids **46**, 1037 (2009).
[67] M. Labousse and J. W. M. Bush, Phys. Fluids **25**, 094104 (2013).